Chinese Chemical Letters 36 (2025) 109630

Contents lists available at ScienceDirect

Chinese Chemical Letters

journal homepage: www.elsevier.com/locate/cclet

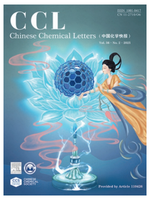

Atomically dispersed Cu-based metal-organic framework directly for alkaline polymer electrolyte fuel cells

Wenbiao Zhang[a,b], Bolong Yang[a], Zhonghua Xiang[a,*]

[a] State Key Laboratory of Organic-Inorganic Composites, Beijing University of Chemical Technology, Beijing 100029, China
[b] Sungrow Hydrogen Sci.&Tech. Co., Ltd., Hefei 230088, China

ARTICLE INFO

Article history:
Received 2 January 2024
Revised 28 January 2024
Accepted 7 February 2024
Available online 14 February 2024

Keywords:
Metal-organic frameworks
Single-metal-site catalysts
Cu-TCNQ/GO
Oxygen reduction reaction
Alkaline polymer electrolyte fuel cells

ABSTRACT

Atomically dispersed Cu-based single-metal-site catalysts (Cu-N-C) have emerged as a frontier for electrocatalytic oxygen reduction reactions (ORR) because they can effectively optimize the ᴅ-band center of the Cu active site and provide appropriate adsorption/desorption energy for oxygen-containing intermediates. Metal-organic frameworks (MOFs) show excellent prospects in many fields because of their structural regularity and designability, but their direct use for electrocatalysis has been rarely reported due to the low intrinsic conductivity. Here, a MOF material (Cu-TCNQ) with highly regular single-atom copper active centers was successfully prepared using a solution chemical reaction method. Subsequently, Cu-TCNQ and graphene oxide (GO) were directly self-assembled to form a Cu-TCNQ/GO composite, which improved the conductivity of the catalyst while maintained the atomically precise controllability. The resistivity of the Cu-TCNQ/GO decreased by three orders of magnitude (1663.6–2.7 W/cm) compared with pure Cu-TCNQ. The half-wave potential was as high as 0.92 V in 0.1 mol/L KOH, even better than that of commercial 20% Pt/C. In alkaline polymer electrolyte fuel cells (APEFCs), the open-circuit voltage and power density of Cu-TCNQ/GO electrode reached 0.95 V and 320 mW/cm^2, respectively, which suggests that Cu-TCNQ/GO has a good potential for application as a cathode ORR catalyst.

The current bottleneck in the development of alkaline polymer electrolyte fuel cells (APEFCs) lies in the slow kinetics of the cathodic oxygen reduction reaction (ORR), which leads to a heavy reliance on precious metal Pt-based catalysts to accelerate the reaction process [1,2]. The high price resulting from low platinum reserves has prompted the search for low-cost, high-performance electrocatalysts. Metal-organic frameworks (MOFs) are a kind of coordination polymers with periodic and infinite network structures formed by the interconnection of metal ions and ligands through self-assembly [3,4]. MOFs are considered as precious metal-free electrocatalytic materials with great development prospects due to their large specific surface area, well-developed pores, tunable chemical composition and surface functions [5]. However, most MOFs are composed of weakly conducting organic ligands that do not provide free carriers and behave as electrical insulators, so their application in the electrocatalytic field remains a great challenge. To address the problem of poor electrical conductivity, most reported strategies for constructing highly active ORR catalysts mainly rely on high-temperature pyrolysis of MOFs to enhance their π-conjugated structure, which often causes undesired structural changes or even destruction, making the highly ordered and tunable MOF structure loses its original advantages [6–10]. Since the original chemical structure of M-N$_x$ is completely destroyed during the pyrolysis process, although the coordination number (x) in M-N$_x$ can be roughly analyzed by X-ray photoelectron spectroscopy (XPS) or X-ray absorption near edge structure (XANES), there is still a large uncertainty. This obvious defect makes it difficult to discover the real active sites and thus to understand the electrocatalytic mechanism. Therefore, how to maintain the clear structure of MOF materials intrinsically ordered is the key to use them for electrocatalytic fields.

Pyrolysis-free MOF-based catalysts can be used to construct interface engineering by choosing appropriate supports, so that the molecular structure of catalysts is controllable and the distribution of catalytic active sites uniform, which provides an effective strategy for further optimizing ORR performance [11–13]. The strong coupling between the oxygen reduction active components and the carrier accelerates the transfer of charges from the active center to the adsorbed reactants/intermediates, and finally changes the overall properties of the composites [14–16]. According to the traditional view of transition metal catalysts, metal atoms are considered as independent active sites. However, with further research,

---

* Corresponding author.
E-mail address: xiangzh@mail.buct.edu.cn (Z. Xiang).

https://doi.org/10.1016/j.cclet.2024.109630

it was found that the local coordination environment around the metal center also plays an important role in ORR performance [17–19]. Therefore, by constructing interfacial engineering to tune the charge density of metal active centers, the stability and activity can be significantly improved [20–22]. For example, Guo *et al.* [23] designed a non-contact scheme of axial carbon substrate induced Fe-N electron localization to enhance its ORR performance. The addition of MWCNTs leads to the aggregation of electron clouds around Fe-N, enhanced the oxygen adsorption capacity and accelerated the ORR rate. Sreekanth *et al.* [24] successfully prepared 3D flower-like Ni-MOF on multi-walled carbon nanotube (MWCNT) by an efficient and rapid microwave synthesis method, exhibiting higher electrochemically active surface area and excellent electrochemical performance compared with pristine Ni-MOF. Apparently, the addition of the conductive carbon matrix further optimizes the redox continuous electron transport path and effectively improves the electrocatalytic ORR activity [25–27].

Herein, we have successfully prepared Cu-TCNQ with highly regular single atom copper active centers by solution chemical reaction using 7,7,8,8-tetracyanoquinodimethane (TCNQ) as inducers. To improve the electrical conductivity of the catalyst while maintaining the ability of atoms to be precisely controlled, we developed a new method to synthesize a hybrid material that directly self-assembles Cu-TCNQ with graphene oxide (GO) into a Cu-TCNQ/GO composite. As a highly conductive two-dimensional material, graphene has high BET specific surface area, large conjugated system, unique high charge mobility and high chemical stability, so combining Cu-TCNQ with graphene significantly improve the charge transfer efficiency of the catalyst. The resistivity was tested by the four-probe method, and the results showed that the resistivity of the Cu-TCNQ/GO composite decreased by three orders of magnitude (1663.6–2.7 W/cm) compared with pure Cu-TCNQ. The ORR activity of the composite was significantly enhanced by the synergistic effect between the highly active Cu-TCNQ and the excellent conductive GO. The half-wave potential was 0.92 V in 0.1 mol/L KOH, which was comparable to state-of-the-art Pt/C electrocatalysts. After 50,000 s of chronoamperometric (*i*-*t*) responses, the current density remained 90% of the original, indicating the good durability of Cu-TCNQ/GO in alkaline solution. In APEFCs, the open-circuit voltage and power density of Cu-TCNQ/GO electrode reached 0.95 V and 320 mW/cm^2, respectively, and the maximum power density was improved by 3.6 times compared with Cu-TCNQ (88 mW/cm^2). This work provides valuable insights into the design and fabrication of novel highly active ORR electrocatalysts without platinum group metals in alkaline media.

To obtain a single-atom catalyst with well-defined M-N$_4$ structure, we chose TCNQ with a coordinated C≡N moiety and periodic structural features as an inducer, and successfully prepared Cu-TCNQ with highly regular single-atom copper active centers by solution chemistry reaction. (Fig. 1a). Single crystal X-ray diffraction results indicate that Cu-TCNQ crystallizes in a monoclinic $P_{2/n}$ space group with Cu$^{\mathrm{I}}$ at the space center. As shown in Fig. S1a (Supporting information), each Cu$^{\mathrm{I}}$ is bound to the nitrogen atoms of four TCNQ ligands. The lengths of the coordination bonds ($d_{\text{Cu-N}}$) were 1.974(2) and 1.954(2) Å, and the bond angle was 109°, which indicates that the Cu$^{\mathrm{I}}$ ion has a slightly distorted octahedral coordination environment [28]. The organic ligand TCNQ connects with the central Cu$^{\mathrm{I}}$ to form a 2D (4, 4) layer [Cu(TCNQ)$_2$]$_\infty$ (Fig. S1b in Supporting information). The 2D (4, 4) layers were infinitely arranged in an ABAB manner, and the Cu$^{\mathrm{I}}$ ions in each layer were located in the center of the grids of the two adjacent layers, and were arranged in an orderly manner along the a-axis from the adjacent layers. Further topological analysis showed that the layers interlaced with each other to form an oblique interpenetrating structure. The two equivalent parallel frameworks were interspersed with each other, finally forming a three-dimensional supramolecular structure (Fig. 1b). It can be seen from the structure that one Cu$^{\mathrm{I}}$ was coordinated with four N to form a Cu-N$_4$ structure, and this abundant, periodically distributed nitrogen-coordinated single-atom copper active center provides a highly active catalytic site.

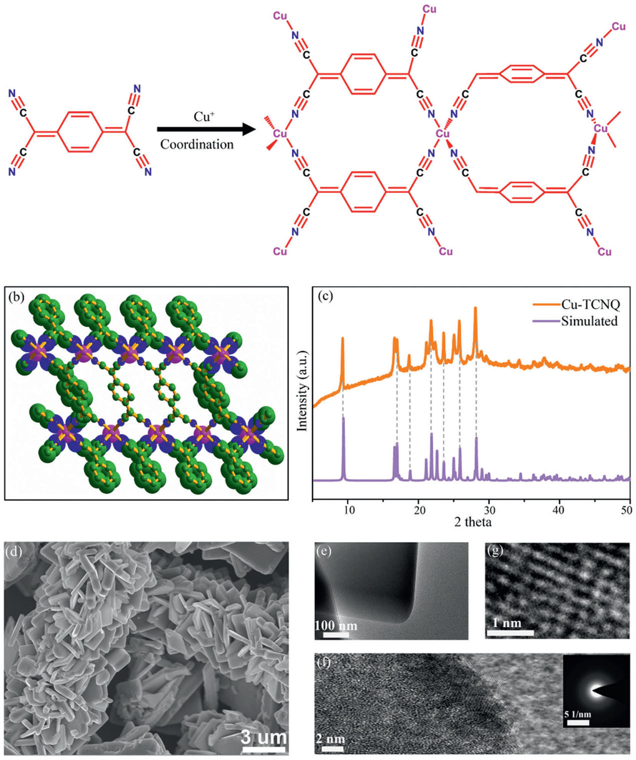

Fig. 1. (a) Synthesis route for Cu-TCNQ. (b) 3D supermolecular framework with 1D channels along the axis in Cu-TCNQ. (c) The simulated and experimental XRD patterns of Cu-TCNQ. (d) SEM image of Cu-TCNQ. (e-g) HRTEM images of Cu-TCNQ, Insets show the SAED analysis.

As shown in Fig. 1c, there were obvious diffraction peaks at 9.4°, 16.62°, 17°, 18.8°, 21.8°, 25.9° and 28.1° in the X-ray diffraction (XRD) curve of the synthesized product, corresponding to (002), (010), (101), (004), (013), (112) and (113) crystal planes of Cu-TCNQ phase, respectively. The peak positions were consistent with those simulated by Cu-TCNQ crystals, and no other impurity peaks were observed, indicating that we successfully synthesized pure Cu-TCNQ samples. The morphology of TCNQ monomer presents irregular bulk, while Cu-TCNQ shows a sheet of about 300 nm (Fig. 1d and Fig. S2 in Supporting information). The reason for the change of morphology was that the process of heating and reflow makes Cu$^{\mathrm{I}}$ coordinate with TCNQ, indicating that we have successfully introduced Cu$^{\mathrm{I}}$ into TCNQ monomer. To further determine the structure, we obtained high-resolution transmission electron microscopy (HR-TEM) images of Cu-TCNQ. The HR-TEM images clearly showed hexagonal pores smaller than 1 nm, arranged in a honeycomb pattern (Figs. 1e-g). The selected area electron diffraction pattern shows that Cu-TCNQ has good (002) and (010) crystal planes, which were in good agreement with the lattice parameters obtained by PXRD. The Fourier transform infrared spectrometer (FTIR) spectrum was shown in Fig. 2a. Compared with the absorption peaks of TCNQ at 861 cm^{-1} (C=C–H bending vibration), 1543 cm^{-1} (C=C stretching vibration in the ring) and 2225 cm^{-1} (C≡N bond stretching vibration), the two sharp absorption bands at 2210 and 2173 cm^{-1} were characteristic peaks of the stretching vibration of the C≡N bond in Cu-TCNQ, and the absorption peak at 1507 cm^{-1} was the stretching vibration peak of the C=C bond in the ring. The shift of the peak positions of the C=C bond and

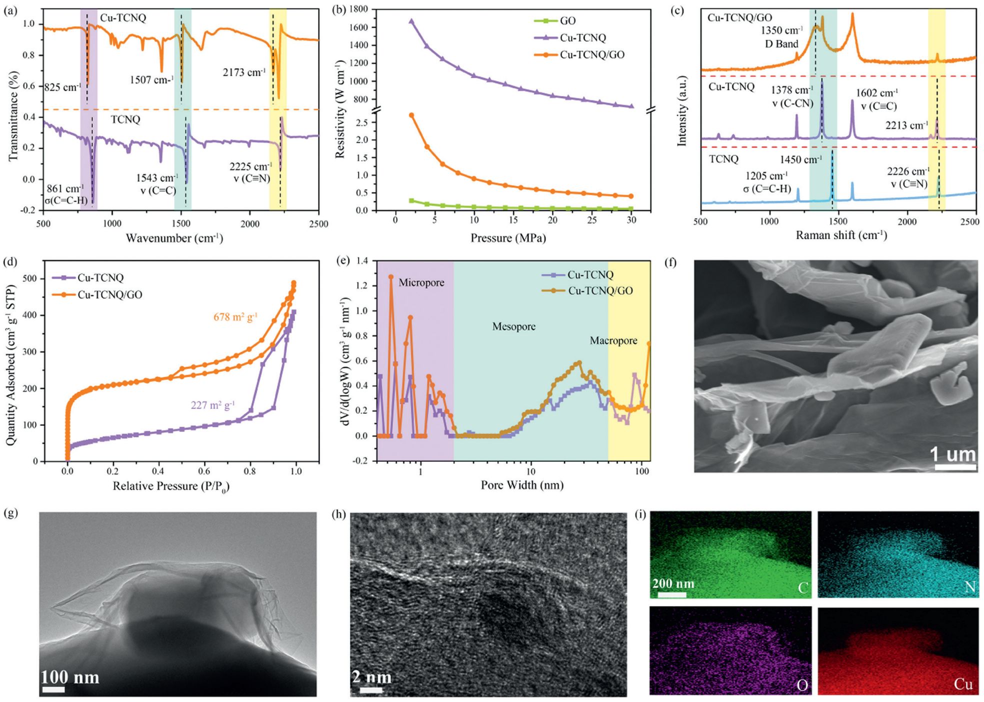

Fig. 2. (a) FT-IR absorption spectra of TCNQ and Cu-TCNQ. (b) Resistivity at different pressures of GO, Cu-TCNQ and Cu-TCNQ/GO. (c) Raman spectra of TCNQ, Cu-TCNQ and Cu-TCNQ/GO. (d) N_2 adsorption-desorption isotherm and (e) pore size distribution curves of Cu-TCNQ and Cu-TCNQ/GO. (f) SEM and (g, h) TEM images of Cu-TCNQ/GO. (i) Elemental mapping images of Cu-TCNQ/GO.

C=C−H bending vibration in the ring indicates that TCNQ has been completely transformed into the $TCNQ^-$ radical anion, and the absorption peaks appearing were all consistent with the literature [29,30]. The FTIR results indicated that the synthesized material was pure Cu-TCNQ phase.

During the ORR reaction, the effect of charge transfer resistance on limiting current density and electrocatalytic performance cannot be ignored. Therefore, to reduce the charge transfer resistance, we supported Cu-TCNQ on GO to obtain the final Cu-TCNQ/GO catalyst. The four-probe resistivity test results show that the resistivity of Cu-TCNQ/GO was greatly reduced compared with Cu-TCNQ, which will greatly accelerate the charge transfer efficiency in the electrochemical reaction process (Fig. 2b). XRD results show that the composite Cu-TCNQ/GO still retains the original coordination structure (Fig. S3 in Supporting information). As shown in the Raman spectrum of Fig. 2c, the main characteristic peaks of TCNQ at 1205 cm^{-1} (C=C−H bending vibration), 1450 cm^{-1} (C−CN bond stretching vibration on both sides of the ring), 1602 cm^{-1} (C=C stretching vibration in the ring) and 2226 cm^{-1} (C≡N bond stretching vibration) were similar to those in the literature [31]. Compared with TCNQ, the stretching vibration peaks of C−CN bond and C≡N bond on both sides of the ring were shifted to 1378 cm^{-1} and 2213 cm^{-1} in Cu-TCNQ, respectively, which indicates that the charge transfer between Cu and TCNQ was completed and Cu-TCNQ was generated. Additionally, the Raman spectrum of Cu-TCNQ/GO detected a distinct peak at 1350 cm^{-1}, which corresponds to the disordered peak of carbon.

Membrane electrode is the core site of APEFCs, which must simultaneously ensure the continuous transmission of electrons, protons and reaction gases, and also ensure the timely discharge of the reaction product water. Therefore, the synthesis of ORR catalysts with high specific surface area and abundant porosity is of great significance for accelerating the transfer efficiency of reaction gases and reaction products and reducing the loss of mass transfer polarization. The nitrogen adsorption-desorption isotherm of Cu-TCNQ/GO showed a typical type IV, and P/P_0 at 0.5–1.0 exhibited a small hysteresis curve due to capillary condensation, which indicated the existence of meso/macroporous structure in Cu-TCNQ/GO (Fig. 2d) [32]. The adsorption capacity increased rapidly at low pressure, which indicated that Cu-TCNQ/GO contained a large number of micropores. The Brunauer-Emmett-Teller (BET) specific surface area of Cu-TCNQ/GO was as high as 678 m^2/g, which was significantly higher than that of pure Cu-TCNQ (227 m^2/g). It can be seen from the pore size distribution diagram that Cu-TCNQ/GO contains both micropores, mesopores and macropores. Such abundant porosity can effectively improve the electrochemical performance of electrode materials (Fig. 2e). Scanning electron microscopy (SEM) image shows that the flake-like Cu-TCNQ was randomly distributed on the surface of graphene, showing a layered and stacked lamellar structure with gaps, which was further illustrated by the TEM image (Figs. 2f and g). HR-TEM images show that Cu was distributed in the porous carbon in the form of single atoms (Fig. 2h). Elemental mapping showed that C, N, O, and Cu were uniformly distributed in the porous carbon (Fig. 2i). Energy dispersive X-ray spectroscopy (EDS) results showed that the content of Cu in Cu-TCNQ and Cu-TCNQ/GO reached 6.17% and 1.13%, respectively (Fig. S5 in Supporting information). The ICP results further accurately confirmed that the Cu content in Cu-TCNQ and Cu-TCNQ/GO were 6.55% and 1.38%, respectively. The existence of higher content of single-atom Cu sites will greatly improve the ORR performance.

Fig. 3a shows the thermogravimetric analysis (TGA) curves of Cu-TCNQ and Cu-TCNQ/GO under N_2 atmosphere at a heating rate of 10 °C/min. Cu-TCNQ experienced two significant weight loss at 150–200 °C and 350–420 °C, which were attributed to the removal of water molecules and the collapse of the carbon skeleton structure, respectively. After the combination of Cu-TCNQ and GO, the weight loss becomes significantly less at the same temperature, which indicates that Cu-TCNQ/GO has good thermal stability. The XPS full spectrum based on Cu-TCNQ and Cu-TCNQ/GO tests

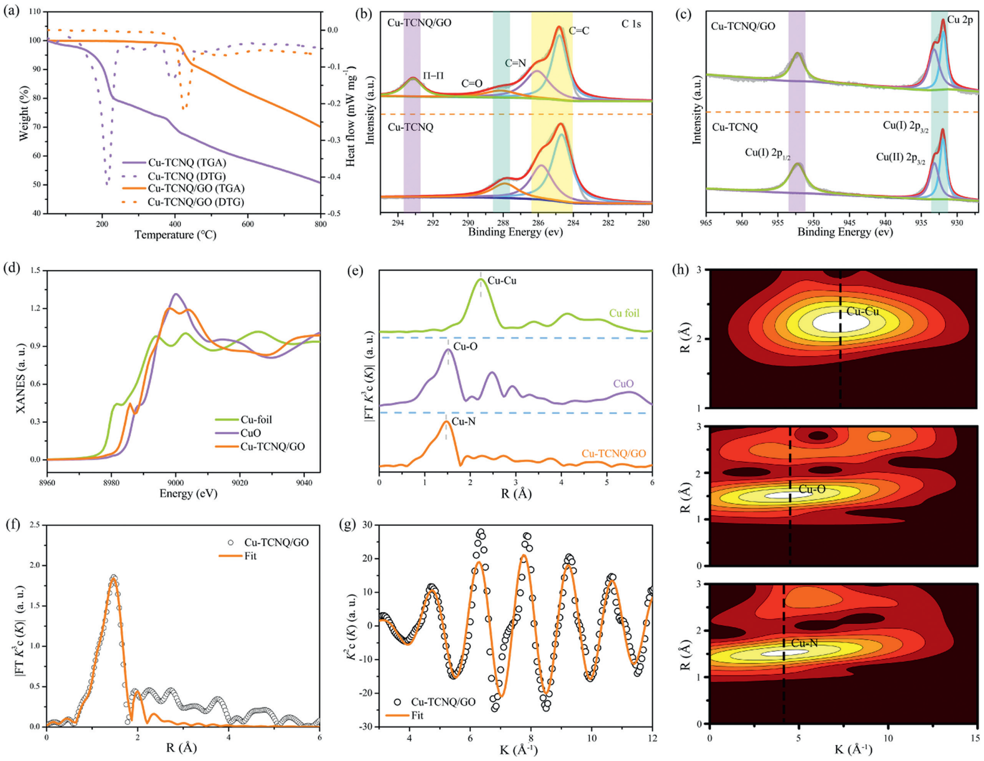

Fig. 3. (a) Thermogravemetric analysis (atmosphere: N_2, rate: 10 °C/min). (b) High resolution C 1s spectra and (c) Cu 2p of Cu-TCNQ and Cu-TCNQ/GO. (d) XANES and (e) EXAFS spectra of Cu-TCNQ/GO, Cu foil and CuO at Cu K-edge. (f) EXAFS fitting curve for Cu-TCNQ/GO at R space. (g) The corresponding EXAFS K space fitting curves. (h) Wavelet transform of EXAFS spectra at Cu K-edge.

showed four distinct peaks at 73.6, 287.5, 398.5 and 532.6 eV, corresponding to the main peaks of Cu 3p, C 1s, N 1s and O 1s, respectively (Fig. S6a in Supporting information). The XPS high-resolution spectra of N 1s indicated that Cu-TCNQ/GO mainly contained N−Cu (398.54 eV) and N−C (400.58 eV) (Fig. S6b in Supporting information) [33]. Additionally, the XPS high-resolution spectra of O 1s indicated that Cu-TCNQ/GO mainly contained C=O (532.02 eV) and C−O (532.95 eV) (Fig. S6c in Supporting information). Besides the C=C, C=N and C=O peaks, another new peak assigned to the Π-Π interaction was observed in the Cu-TCNQ/GO spectrum (Fig. 3b). As expected, the similar Cu 2p peaks in the spectra of Cu-TCNQ and Cu-TCNQ/GO also demonstrate the successful binding of Cu-TCNQ and graphene and the preservation of active sites (Fig. 3c).

The interfacial structure has been investigated at atomic scale using X-ray absorption near-edge structure (XANES) and extended X-ray absorption fine structure (EXAFS). The position of the Cu k-edge absorption threshold reflects the average valence state of Cu. The Cu k-edge XANES spectrum in Fig. 3d suggests that the oxidized valence state of the isolated single Cu atom in Cu-TCNQ/GO may be higher than that of metallic Cu^0 and lower than that of Cu^{2+}, an observation that is consistent with the XPS results. In the EXAFS spectra of Cu_2O and CuO, the peaks at 1.52 and 2.24 Å belong to Cu-O and Cu-Cu coordination, respectively (Fig. 3e) [34–36]. The EXAFS curve of the Cu-TCNQ/GO sample shows the main peak at about 1.46 Å, which is due to scattering interactions between the Cu atoms and the first shell layer (Cu-N). No Cu-Cu characteristic peaks were detected, which implies that copper is atomically dispersed on the catalyst. Quantitatively, the structural parameters of the Cu k-edge were extracted using least squares EXAFS fitting (Figs. 3f and g). The results show that the first layer of the central atom Cu has a coordination number of 4, thus forming a Cu-N_4 active center. The detailed fitting parameters were shown in Table S3 (Supporting information). The atomic configuration of Cu-TCNQ/GO has been investigated using the Cu k-edge wavelet transform (WT) due to the strong resolution in k-space and R-space (Fig. 3h). Strong coordination of Cu-Cu (~7.1 $Å^{-1}$) and Cu-O (4.2 $Å^{-1}$) was observed in the WT contour plots of Cu foils and CuO, which was in agreement with the results of EXAFS spectroscopy. No Cu-Cu coordination was observed in Cu-TCNQ/GO compared to the WT signal of Cu foil, which further confirming the isolated feature of Cu species. These results further indicate that we successfully synthesized Cu-TCNQ/GO catalysts with well-defined Cu-N_4 structures.

The electrocatalytic activity of the catalysts was evaluated using a typical three-electrode system in N_2/O_2 saturated 0.1 mol/L KOH solution. The cyclic voltammetry (CV) curve of Cu-TCNQ/GO in O_2 showed a distinct reduction peak, indicating the occurrence of electrocatalytic reaction (Fig. 4a) [37]. We firstly explored the effect of different contents of GO on the ORR activity and showed that the best electrochemical performance was achieved at a Cu-TCNQ to GO ratio of 1:2.4 (Fig. S7 in Supporting information). The reason was that when a small amount of GO was added, the electron transfer and mass transport were affected due to poor conductivity, and when an excess of GO was added, the number of Cu active sites decreases significantly, thus affecting the catalytic performance. As expected, the linear sweep voltammetry (LSV) curves of TCNQ in O_2-saturated 0.1 mol/L KOH solution showed little catalytic activity (Fig. 4b). On the contrary, the LSV curve corresponding to Cu-TCNQ/GO exhibited excellent ORR activity with an onset potential (E_{onset}) of 1.03 V and a half-wave potential ($E_{1/2}$) of 0.92 V (vs. RHE), which were significantly higher than that of pure Cu-TCNQ (E_{onset}=0.94 V) and ($E_{1/2}$=0.87 V), even higher than commercial 20% Pt/C (E_{onset}=1.01 V, $E_{1/2}$=0.9 V). Additionally, the excellent electrocatalytic performance of Cu-TCNQ/GO was higher than that of ORR catalysts reported in most of the previous literatures (Table S4 in Supporting information). The kinetic

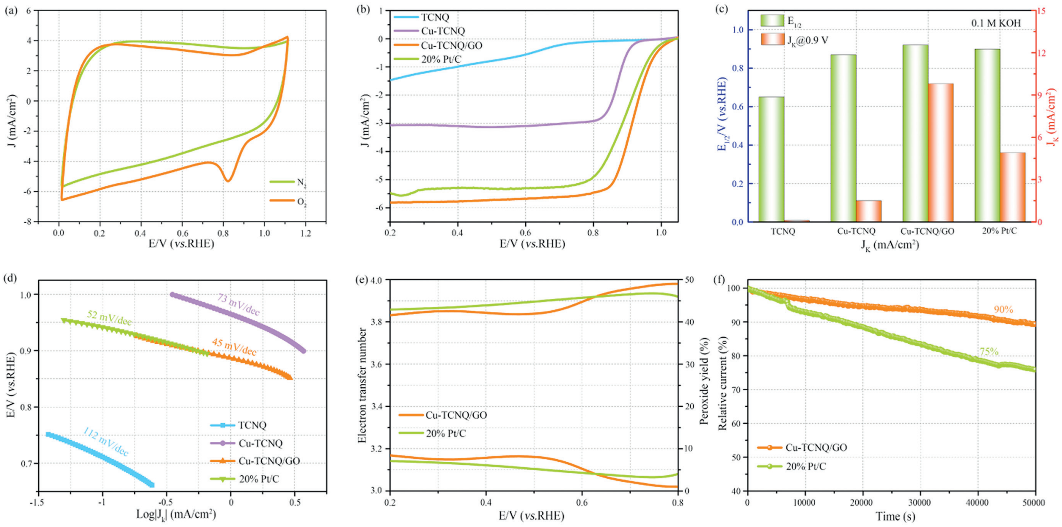

Fig. 4. (a) CV curves in 0.1 mol/L N_2/O_2-saturated KOH solutions at 100 mV/s. (b) ORR polarization curves of different catalysts. (c) The corresponding J_k at 0.75 V and $E_{1/2}$. (d) The corresponding Tafel slopes. (e) Electron transfer number and H_2O_2 yield plots of Cu-TCNQ/GO and 20% Pt/C. (f) Chronoamperometric (*i*-*t*) responses of Cu-TCNQ/GO and 20% Pt/C (rotation rate: 1600 rpm).

current density (J_k) of Cu-TCNQ/GO catalyst was calculated to be 9.8 mA/cm^2 at 0.9 V using the Koutecky-Levich (K-L) equation, which were much higher than those of TCNQ, Cu-TCNQ and commercial 20% Pt/C (Fig. 4c). Moreover, the limiting current density of Cu-TCNQ/GO was significantly improved compared to Cu-TCNQ, which was due to the presence of graphene that enhances the conductivity of the catalyst. The variation is also consistent with the changes in mass activity. As shown in Fig. S8 (Supporting information), Cu-TCNQ/GO exhibits the highest mass activity with 38.5 mA/mg at 0.9 V. The Tafel slope of Pt/C was 52 mV/dec, and the lower Tafel slope (45 mV/dec) further demonstrates the excellent ORR activity of Cu-TCNQ/GO, indicating that the reaction mechanism of ORR on the catalyst surface was similar to that of Pt (Fig. 4d). Cu-TCNQ/GO showed an efficient four-electron reaction pathway and very low hydrogen peroxide yield, almost the same as commercial 20% Pt/C, as measured by rotating ring-disk electrode (RRDE) (Fig. 4e). The LSV curves of Cu-TCNQ/GO at different rotational speeds were shown in Fig. S9a (Supporting information). The K-L equation calculation shows that the electron transfer numbers at different potentials show a process close to four-electron transfer, which was consistent with the RRDE test results (Fig. S9b in Supporting information). Additionally, the double-layer capacitance (C_{dl}) is related to the electrochemically active specific surface area of the electrocatalyst, which can be obtained from the CV curves (non-Faraday reaction regions) at different scan rates (Figs. S10a and b in Supporting information) [38]. As shown in Fig. S10c (Supporting information), the C_{dl} value of Cu-TCNQ/GO is 110 mF/cm^2, which was significantly higher than that of Cu-TCNQ (16 mF/cm^2), and these results also indicate that Cu-TCNQ/GO has a good ORR catalytic performance. Cu-TCNQ/GO also showed superior stability, with the current density remaining 90% of the original after 50,000 s of chronoamperometric (*i*-*t*) responses, which was significantly higher than that of commercial Pt/C (Fig. 4f).

The enhanced activity of the Cu-TCNQ/GO catalyst was mainly attributed to the synergistic interaction between the highly conductive graphene and Cu-TCNQ with abundant active sites. Graphene has good electrical conductivity, which reduces the resistivity of the composite and provides a highly conductive pathway for electron transfer. On the other hand, the Cu-TCNQ catalyst maintains good structure and composition with abundant N content, which provides sufficient active sites for ORR.

To further evaluate the performance of Cu-TCNQ and Cu-TCNQ/GO catalysts in APEFCs, the corresponding membrane electrode assembly (MEAs) were prepared and assembled into APEFCs. The specific test device was shown in Fig. 5a. The effects of back pressure and the loading of cathode catalysts on the performance of fuel cells were first explored. As shown in Fig. S11a (Supporting information), the performance of APEFCs was obviously improved with the increase of back pressure, which was due to the presence of back pressure accelerates the reaction rate of H_2/O_2. Additionally, with the increase of cathode catalyst loading, the performance of APEFCs showed a trend of first increasing and then decreasing (Fig. S11b in Supporting information). This was due to the number of active sites in the catalyst increases with the increase of the content at first, so the power density improved. As the loading continues to increase, the number of active sites of the catalyst also increases. However, the thick membrane electrode makes the transfer rate of electrons, protons and reaction gases slow, and many active sites cannot be fully utilized, thus reducing the performance of APEFCs. Therefore, after exploration, we set the test conditions of the fuel cell as follows: cathode catalyst loading: 3 mg/cm^2, anode: 0.2 mg$_{Pt}$/cm^2, H_2/O_2: 0.4/0.8 L/min, backpressure: 2 bar, electrode area 5 cm^2, temperatures: 80 °C. The polarization curve shows that the open-circuit voltage and power density of Cu-TCNQ/GO reach 0.95 V and 320 mW/cm^2, respectively (Fig. 5b). Compared with Cu-TCNQ (88 mW/cm^2), the maximum power density was increased by 3.6 times, which was higher than the performance of most previously reported cathodic catalysts APEFCs (Table S5 in Supporting information). The corresponding Tafel slope also indicates that Cu-TCNQ/GO has excellent APEFCs performance (Fig. 5c). Moreover, the performance of APEFCs was evaluated in H_2/air system to be closer to the actual fuel cell operation state, and the results showed that the maximum power density of Cu-TCNQ/GO reached 160 mW/cm^2, which was significantly higher than that of Cu-TCNQ (Fig. S12 in Supporting information).

The transfer kinetics of the as-prepared fuel cells were verified by Nyquist plot (Fig. 5d), where the value of the initial intersection with the x-axis represents the charge transfer resistance (R_{ct}) of the APEFCs, and the diameter of the semicircle represents the total ohmic resistance (R_{ohm}). It is noticeable that Cu-TCNQ/GO cathodes exhibit much smaller R_{ct} (0.012 Ω/cm^2) and R_{ohm} (0.03 Ω/cm^2) *vs.* Cu-TCNQ (R_{ct}=0.014 Ω/cm^2, R_{ohm}=0.87 Ω/cm^2) catalysts. This indicates that the presence of graphene can improve the electrical con-

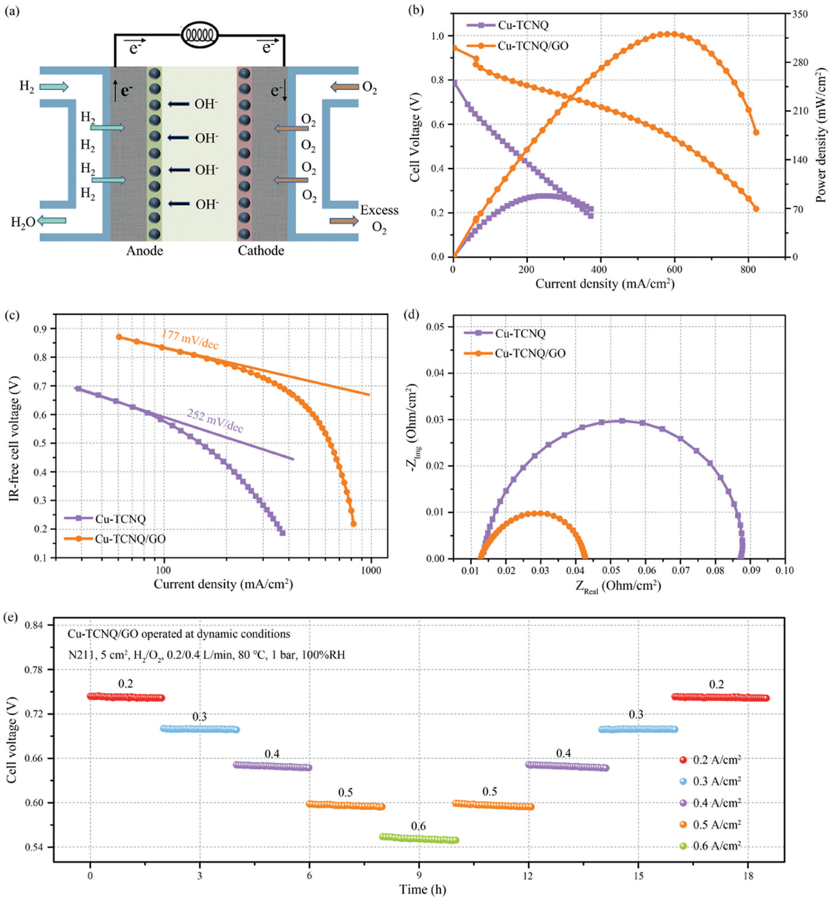

Fig. 5. (a) Diagram of a single battery tests. (b) H_2–O_2 APEFCs with the prepared materials as the cathode catalysts. Membrane: alkaline polymer membrane, cathode catalyst loading: 3 mg/cm^2, anode: 0.2 mg$_{Pt}$/cm^2, H_2/O_2: 0.4/0.8 L/min, backpressure: 2 bar, electrode area 5 cm^2, temperatures: 80 °C. (c) The corresponding Tafel plots. (d) Nyquist plots for PEMFCs at 0.5 A/cm^2. (e) The stability of dynamic cyclic process for Cu-TCNQ/GO electrode.

ductivity of the composite and reduce the mass transfer resistance of charge. Besides high catalytic activity, long lifetime is another key factor to ensure the application of APEFCs. We test the open circuit voltage with time by continuously changing the current density. Compared with the traditional stability test, the durability test conditions of this dynamic cycle process were more demanding. The results show that the open circuit voltage of the fuel cell can still return to the original state after cycling tests at different current densities, which indicates that Cu-TCNQ/GO electrode has excellent cyclic stability (Fig. 5e). The morphology of Cu-TCNQ/GO did not change after the stability test, and the TEM images also showed that Cu-TCNQ/GO did not aggregate on the graphene surface (Fig. S13 in Supporting information). Additionally, the XRD of Cu-TCNQ/GO after the stability test was consistent with that before the test, and the Cu 2p spectrum contains the same peaks as the as-prepared catalyst (Figs. S14 and S15 in Supporting information). The above results confirm that the structure of Cu-TCNQ does not change, which was the main reason for the excellent stability of the catalyst.

We successfully prepared Cu-TCNQ with periodically distributed single-atom copper active centers by solution chemical reaction method using TCNQ and Cu^{I} as ligand and metal center, respectively. It can be seen from the structure that one Cu^{I} was coordinated with four N atoms to form a Cu-N$_4$ structure, and this abundant and highly regular nitrogen-coordinated single-atom copper active center provides a highly active catalytically site. To improve the electrical conductivity of the catalyst while maintaining the atomically precisely controllable ability, we developed a new method to synthesize a hybrid material that directly self-assembles Cu-TCNQ with GO into a Cu-TCNQ/GO composite. The four-probe test results showed that the resistivity of Cu-TCNQ/GO composites decreased by three orders of magnitude (1663.6–2.7 W/cm) compared with pure Cu-TCNQ. Due to the synergistic interaction between highly conductive graphene and Cu-TCNQ with abundant active sites, Cu-TCNQ/GO exhibited excellent electrocatalytic ORR activity with a half-wave potential as high as 0.92 V in 0.1 mol/L KOH. When Cu-TCNQ/GO was used as the cathode catalyst of APEFCs, the maximum power density of the fuel cell reaches 320 mW/cm^2, which was 3.6 times higher than that of Cu-TCNQ (88 mW/cm^2). This work provides a new insight into the design of cost-effective MOF-based ORR electrocatalysts.

Declaration of competing interest

The authors declare that they have no known competing financial interests or personal relationships that could have appeared to influence the work reported in this paper.

Acknowledgments

This work was supported by the National Key Research and Development Program of China (No. 2022YFB3807500), the National Natural Science Foundation of China (No. 22220102003), the Beijing Natural Science Foundation (No. JL23003), “Double-First-Class” construction projects (Nos. XK180301 and XK1804–02).

Supplementary materials

Supplementary material associated with this article can be found, in the online version, at doi:10.1016/j.cclet.2024.109630.

References

[1] B.L. Yang, X.L. Li, Q. Cheng, et al., Nano Energy 101 (2022) 107565.
[2] Q.H. Li, H.Q. Peng, Y.M. Wang, et al., Angew. Chem. Int. Ed. 58 (2019) 1442–1446.
[3] P. Qin, S. Zhu, M. Mu, et al., Chin. Chem. Lett. 34 (2023) 108620.
[4] B.L. Yang, B.J. Li, Z.H. Xiang, Nano Res. 16 (2023) 1338–1361.
[5] Y. Wang, Y. Pan, L.K. Zhu, et al., Carbon 146 (2019) 671–679.
[6] F. Zhang, X. Liu, Y. Chen, et al., Chin. Chem. Lett. 34 (2023) 108142.
[7] G.B. Chen, P. Liu, Z.Q. Liao, et al., Adv. Mater. 32 (2020) 1907399.
[8] X.Y. Xie, L.S. Peng, H.Z. Yang, et al., Adv. Mater. 33 (2021) 2101038.
[9] Y.J. Chen, S.F. Ji, Y.G. Wang, et al., Angew. Chem. Int. Ed. 56 (2017) 6937–6941.
[10] J. Qiao, Z. Bao, L. Kong, et al., Chin.e Chem. Lett. 34 (2023) 108318.
[11] H.X. Zhong, K.H. Ly, M.C. Wang, et al., Angew. Chem. Int. Ed. 131 (2019) 10787–10792.
[12] B.L. Yang, Q. Han, L.K. Han, et al., Adv. Mater. 35 (2023) 2208661.
[13] M.H. Liu, S.J. Liu, C.X. Cui, et al., Angew. Chem. Int. Ed. 61 (2022) e202213522.
[14] R. Bao, Z.H. Xiang, Z.L. Qiao, et al., Angew. Chem. Int. Ed. 62 (2023) e202216751.
[15] B.L. Yang, H.F. Yu, X.D. Jia, et al., ACS Appl. Mater. Interfaces 15 (2023) 23316–23327.
[16] K.M. Zhao, S.Q. Liu, Y.Y. Li, et al., Adv. Energy Mater. 12 (2022) 2103588.
[17] X.L. Li, Z.H. Xiang, Nat. Commun. 13 (2022) 57.
[18] C. Zhang, B. An, L. Yang, et al., J. Mater. Chem. A 4 (2016) 4457–4463.
[19] S.H. Liang, R.J. Chen, P.W. Yu, et al., Chem. Commun. 53 (2017) 11453–11456.
[20] I.E.L. Stephens, J. Rossmeisl, I. Chorkendorff, Science 354 (2016) 1378–1379.
[21] K. Jiao, J. Xuan, Q. Du, et al., Nature 595 (2021) 361–369.
[22] X.X. Wang, M.T. Swihart, G. Wu, Nat. Catal. 2 (2019) 578–589.
[23] Z.Y. Mei, S. Cai, G.F. Zhao, et al., Chem. Eng. J. 430 (2022) 132691.
[24] T.V.M. Sreekanth, G.R. Dillip, P.C. Nagajyothi, et al., Appl. Catal. B: Environ. 285 (2021) 119793.
[25] S.J. Liu, M.H. Liu, X.W. Li, et al., Carbon Energy 5 (2023) 1–11.
[26] K.Y. Zou, M.Z. Jiang, Z.X. Zhao, et al., Chem. Eng. J. 476 (2023) 146793.
[27] R. Ren, L.T. Yang, Z. Lin, et al., J. Mater. Chem. A 10 (2022) 22781–22790.
[28] D. Wu, Y.C. Wei, X. Ren, et al., Adv. Mater. 30 (2018) 1705366.
[29] Z.Q. Deng, C.Q. Ma, S.H. Yan, et al., J. Mater. Chem. A 9 (2021) 20345–20349.
[30] J. Ma, E. Zhou, C. Fan, et al., Chem. Commun. 54 (2018) 5578–5581.
[31] Q. Li, P.F. Yan, G.F. Hou, et al., Dalt. Trans. 42 (2013) 7810–7815.
[32] K.Y. Zou, Z.R. Song, X. Gao, et al., Angew. Chem. Int. Ed. 60 (2021) 17070–17079.
[33] B.L. Yang, J.K. Hou, Y.Y. Mi, et al., Next Sustain. 2 (2023) 100014.
[34] T. Yang, X.N. Mao, Y. Zhang, et al., Nat. Commun. 12 (2021) 6022.
[35] Y.T. Qu, Z.J. Li, W.X. Chen, et al., Nat. Catal. 1 (2018) 781–786.
[36] T. Wang, R. Yang, N.E. Shi, et al., Small 15 (2019) 1902410.
[37] Z. Wang, C. Zhu, H. Tan, et al., Adv. Funct. Mater. 31 (2021) 2104735.
[38] J. Yang, W.G. Liu, M.Q. Xu, et al., J. Am. Chem. Soc. 143 (2021) 14530–14539.